A true triaxial experimental study on porous Vosges sandstone: from strain localization precursors to failure using full-field measurements

Cyrille Couture, Pierre Bésuelle

A true triaxial experimental study on porous Vosges sandstone: from strain localization precursors to failure using full-field measurements

Cyrille Couture and Pierre Bésuelle

Univ. Grenoble Alpes, CNRS, Grenoble INP, 3SR, 38000 Grenoble, France

---

Abstract

This study systematically investigates the effect of deviatoric loading paths on diffuse and localized deformation developing during the mechanical loading of a high porosity (20%) Vosges sandstone (Eastern France). Laboratory scale experiments are performed using a high pressure true triaxial apparatus, designed to provide access to full-field surface kinematics at high spatial and temporal resolutions during the loading phase. The true triaxial experiments, with independent control of the three principal stress, are conducted at two constant mean stresses, in the brittle-ductile transition regime, and at five prescribed Lode angles, from axisymmetric compression (ASC) to axisymmetric extension (ASE). First, the transition from diffuse towards localized deformation is analyzed in different loading increments and shows an intermediate step of early strain localization, characterized by a large number of early deformation bands developing well before the stress peak and with a predominantly dilatant behavior. Secondly, the evolution of the mechanical behavior and localization patterns, such as deformation band angles and localized dilatancy, indicate a transition from the brittle regime to the ductile regime that is not only dependent on an increase in the mean stress, but also on a decrease in the Lode angle. The analysis of full-field measurements also provides insights into the emergence and evolution of local strains, as deformation structures coalesce or relocate and different failure modes develop depending on the prescribed stress paths.

Keywords: true triaxial experiments, strain localization, full-field measurements, localization precursors, Lode angle, sandstone, porous rock

---

1. General context

The development of strain localization in confined geomaterials is recognized as a fundamental deformation mechanism which generally relates to an evolution in the mechanical response and failure. In high porosity sandstone, this phenomenon is most often apparent in the form of a unique or series of parallel and conjugated deformation bands, characterized by extended structural deformations in narrow and linear zones of concentrated deformation [e.g., 1, 2, 3].

In studies performed under controlled laboratory settings, the manifestation of deformation bands leading to failure in stressed rock samples has been demonstrated to be sensitive to the loading path and the mechanical response of the underlying micro-structure. A well studied phenomenon in high porosity rocks is the transition into a ductile regime with an increase in the first invariant of the stress tensor, i.e. the mean stress [e.g., 4, 5]. The conventional triaxial apparatus, where a stress deviator is applied in the major principal direction while the confining pressure is applied on a jacketed cylindrical specimen, is well suited to assess the role of the mean stress. In such experimental conditions, the apparatus-sample contact boundaries are well defined, by the superposition of a confining fluid and a deviatoric loading using an axial unidirectional rigid piston. Nonetheless, the lack of independent control between the radial stresses limits the imposed stress paths to axisymmetric compression and extension conditions, leaving an intermediate broad spectrum of the octahedral (deviatoric) plane unexplored.

To circumvent this limitation, different variations of the true triaxial apparatus (TTA) have been developed in various experimental laboratories, aiming to investigate the role of alternative stress paths to the classical axisymmetric cases [6]. The most prominent method for mechanical testing of rocks in true triaxial conditions consists in performing loading experiments at different minor and intermediate principal stress levels, while the major principal stress evolves with incremental axial strain. As such, the design advancements of the TTA have enabled to demonstrate the important role of the intermediate principal stress on the deformation and failure mechanisms in various types of rocks. In terms of the resulting stress invariants during this type of loading, while intermediate values of the Lode angle, between 0° and 60°, can be achieved, the Lode angle continuously and systematically decreases in conjunction with an increase in the mean stress (σ_m). Therefore, the independent effect of the stress invariants on the evolution of the material response cannot be directly assessed. Additionally, their continuous and simultaneous evolution during loading, inherent to principal stress controlled loading, results in the distribution of stress states at failure to be scattered in certain regions of the meridian and octahedral planes. Figures 1a.-l. illustrates this effect for selected data sets retrieved from the literature for principal stress controlled testing of various rock samples, where values of the peak octahedral stress, as defined in equation 1, are represented as projections on a single octahedral plane.

An alternative experimental approach consists in systematically investigating different stress paths with prescribed invariants of the stress tensor, by imposing an incremental relation between the principal stresses. Experiments performed under this type of loading procedure provide valuable insight on the independent effect of isotropic and deviatoric loading paths on the mechanical response and deformation mechanisms. Ingraham et al. [13] performed a series of experiments under such loading conditions on samples of a high porosity sandstone, by imposing two independent invariants during the loading phase: the mean stress (σ_m) and the Lode angle (θ), as defined in equation 1. The peak stress recorded for each test are thus organized on selected meridian and deviatoric planes (see Figure 1.m). Ma et al. [14] have followed a similar methodology, for a mixed loading mode at a constant minor principal stress and constant Lode angle in two different porous sandstone samples. The results from these two studies have consistently shown a measurable effect of the Lode angle on failure and localization patterns analyzed in post-mortem observations. Nonetheless, experimental data on the subject are scares and many questions remain open as to the mechanisms involved during the deformation process of porous rocks subjected to general stress paths.

It is thus essential to further study the effect of different loading conditions in terms of the mechanical response, but also in their relation to the emergence and development of localization structures in porous rocks. The purpose of the present experimental campaign is therefore to systematically explore the effect of different invariant controlled stress paths on the mechanical response, combined with a unique full-field measurement technique to characterize the diffuse and localized deformation in laboratory samples of a Vosges sandstone, a high porosity quasi-isotropic model sedimentary rock.

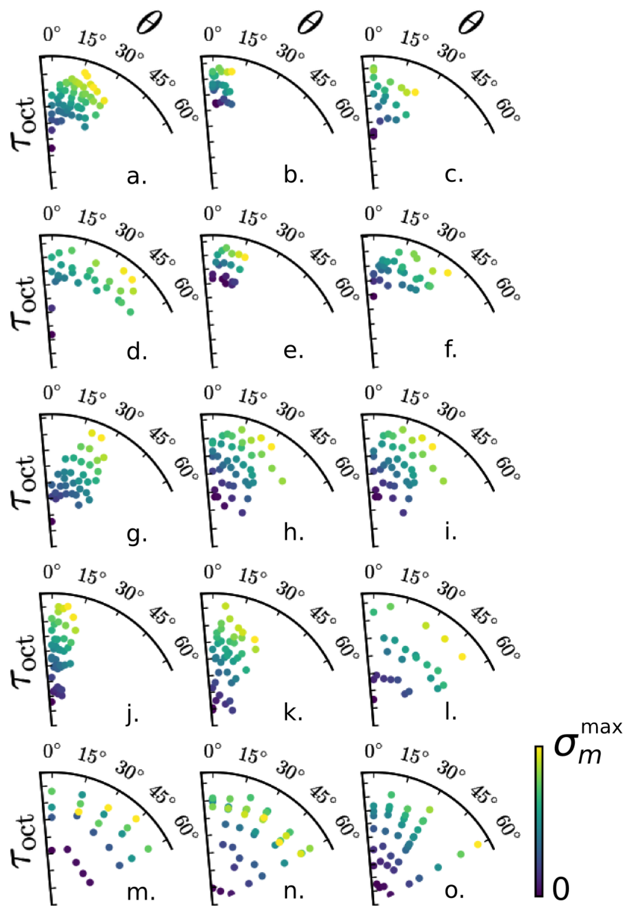

Figure 1: Representation of stress state at failure in the octahedral plane, arranged by experimental campaigns retrieved from the literature: Dunham dolomite (a), Inada granite (b), Manazuru andesite (c), Mizuho trachyte (d), Orikabe monzonite (e), Solhofen limestone (f), Yamaguchi marble (g) [from 7]; Yuubari shale (h), Shirahama (i) [8] [data from 9]; Westerly granite (j) [10]; KTB amphibolite (k) [11]; Taiwan siltstone (l) [12]; Castlegate sandstone (m) [13]; Coconino sandstone (n), Bentheim sandstone (o) [14] . The color scale indicates the mean stress level reached at the deviatoric stress peak, the value of the maximum mean stress being specific to each study.

2. Methods and material

2.1. Experimental setup

The high pressure true triaxial apparatus (TTA) used for this experimental campaign has been designed and assembled at Laboratoire 3SR (Grenoble) for the specific purpose of testing rock samples in biaxial and true triaxial loading conditions [15]. The apparatus is designed to accommodate prismatic samples of $50 \times 30 \times 25$ mm^3 inside a specially fabricated soft membrane installed in the main confining chamber. The loading mechanism of this apparatus relies on a combination of direct fluid pressure and a pair of rigid pistons to apply stresses at the surfaces of the prismatic samples. The mixed boundary conditions aligned with the surfaces of the sample are thus imposed by a combination of rigid stainless steel and sapphire glass contacts in the major (1) and intermediate (2) directions, respectively; and a soft contact through the jacket in the minor (3) direction. The loading device is rated for a maximum isotropic confinement of up to 100 MPa, applied by increasing the fluid pressure inside the confining chamber hosting the isolated sample. The stress deviators, decoupled in the major and intermediate directions, are applied by the means of pressure controlled hydraulic pistons (self-equilibrated with respect to the cell pressure). In the major direction 1, a set of sliding pedestals transfer the load on the surface of the specimen while accommodating displacements in the orthogonal direction. For the specified sample dimensions and through the effect of the balanced ram, the stress deviator, in both the major and intermediate directions, can reach up to 670 MPa and 530 MPa, respectively. A detailed description of the apparatus is given in [16]. A recent modification consist in the manufacturing of urethane molding rubber to produce soft reusable jackets, making them adaptable to strain gauge installation by passing cable through sealed conduits; an essential improvement to obtain direct surface strain measurements in the out-of-plane (non-visible) direction 2 [17].

2.2. Loading Procedure

Using linear relationships between the principal stress values (σ_1, σ_2 and σ_3), a loading procedure was developed for the control system of the apparatus to perform true triaxial loading experiments with imposed loading paths based on the invariants of the Cauchy stress tensor. While any combination of mutually independent set of invariants are suitable to objectively define general stress state increments, the Octahedral-Lode invariants is preferred as it describes a convenient polar coordinate system around the trisectrix, or isotropic stress state line, in the principal stress space. The selected invariants are thus defined as

$$\begin{aligned}
\sigma_{av} &= \frac{1}{3}[\sigma_1 + \sigma_2 + \sigma_3] \\
\tau_{oct} &= \frac{1}{3}\left[(\sigma_1 - \sigma_2)^2 + (\sigma_1 - \sigma_3)^2 + (\sigma_2 - \sigma_3)^2\right]^{1/2} \\
\theta_\sigma &= \arctan\left[\sqrt{3}\frac{\sigma_2 - \sigma_3}{(\sigma_1 - \sigma_2) + (\sigma_1 - \sigma_3)}\right]
\end{aligned} \quad (1)$$

where σ_{av} is the average stress, and τ_{oct} and θ are respectively the octahedral stress and Lode angle, measuring independently the deviatoric stress magnitude and orientation in the octahedral plane (see Figure 2). The strain invariants (ϵ_{av}, γ_{oct}, θ_ϵ) are equivalently defined in terms of the principal values of the strain tensor. In the adopted solid mechanics convention, compatible with the presented full-field measurements, both principal stresses and strains are positive in tension. To simplify the discussion of results, the invariants along the trisectrix of the principal stress and strain space are presented in terms of the mean stress, $\sigma_m = -\sigma_{av}$, and the volumetric strain, $\epsilon_v = 3\epsilon_{av}$. Therefore σ_m is positive in compression and ϵ_v is positive during dilatancy. The Lode angle, as defined in equation 1, spans from 0^o in axisymmetric compression (ASC, $\sigma_2 = \sigma_3$) to 60^o in axisymmetric extension (ASE, $\sigma_1 = \sigma_2$). It is a measure of the deviatoric stress orientation in the stress space, and can be intuitively interpreted as an indication of the intermediate principal stress magnitude, with respect to the magnitude of the minor and major principal stresses at a given mean stress.

For the presented experimental campaign, a consistent procedure was followed for each experiment performed at prescribed loading paths: (1) a sample alignment phase is initiated to insure centering of the contact between the pistons, pedestals and the sample surfaces in directions 1 and 2; (2) a subsequent isotropic monotonic loading phase consists of increasing the cell pressure at a rate of 2 MPa/min, until the prescribed mean stress is reached; (3) finally, a deviatoric loading phase consists in monotonically increasing the octahedral stress while maintaining σ_m and θ at constant values. During this last loading phase, a PID controller feedback loop prescribes the hydraulic pressure to update the intermediate and minor principal stresses, in terms of the major principal stress, according to the relationship:

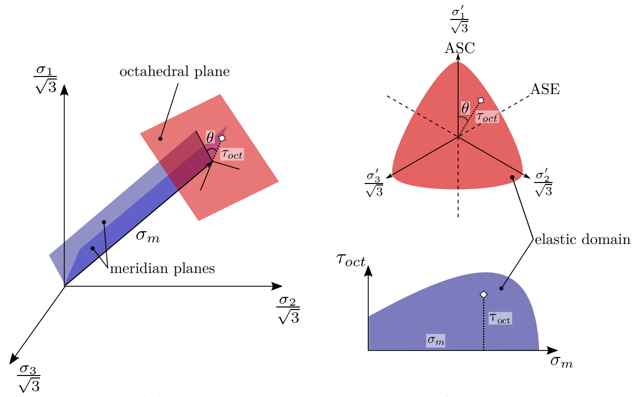

(a) (b)

Figure 2: A graphical representation of the cylindrical Lode coordinate system in the principal stress space (a), based on the three invariants σ_m, τ_{oct} and θ. In (b), the octahedral plane (normal projection on a plane perpendicular to the isotropic state line) and the meridian plane (τ_{oct} vs. σ_m) provide complementary 2D information of the stress state.

$$
\begin{aligned}
\sigma_2 &= \frac{3\tan\theta - \sqrt{3}}{2\sqrt{3}}\,(\sigma_1 - \sigma_m) + \sigma_m \\
\sigma_3 &= \frac{-3\tan\theta - \sqrt{3}}{2\sqrt{3}}\,(\sigma_1 - \sigma_m) + \sigma_m
\end{aligned}
\tag{2}
$$

obtained from a simple algebraic rearrangement of equations 1. The hydraulic syringe pumps are controlled based on this set of equations, while including additional proportionality parameters to calibrate the hydraulic pressure in the piston according to the sample surface stresses and frictional correction terms. These linear correction terms take into account the variation in the dynamic friction effect between the piston shaft and the seals with the variation in hydraulic pressure in the main confining chamber, which is equal to σ_3. The correction of σ_1 ranges from 4.6 MPa to 9.7 MPa and the correction σ_2 from 3.2 MPa to 9.3 MPa, for values of σ_3 between 0 MPa and -90 MPa.

Due to significant non-linear elastic deformation of the apparatus during the deviatoric loading phase, the vertical strain rate could not be explicitly prescribed based on the measurements from the external LVDT linked to the control system. The exact strain measurements are therefore a priori

Table 1: Mineral characterization of Vosges sandstone

mineral composition	93% quartz
	5% microcline
	2% mica and kaolinite
porosity	21%
grain size	150-450 μm
mean grain size	300 μm

unknown during the experiments, since applied corrections from the sample boundary displacement are obtained by digital image correlation during the post-experimental analysis. Instead, the monotonic loading in the major principal direction is controlled at a constant injection rate (1.5 cc/hr) in the vertical piston chamber, resulting in a mean vertical strain rate for all the experiments of $4.2 \times 10^{-7}\,\mathrm{s}^{-1}$ at the beginning of the deviatoric loading phase and $2.3 \times 10^{-6}\,\mathrm{s}^{-1}$ at the end of the hardening phase. This strain rate evolution during the experiment is a function of the compressibility of the injection fluid, an hydraulic oil with entrapped air pockets, and the stiffness of the true triaxial apparatus.

2.3. Material

A total of ten samples has been prepared using a single block of Vosges sandstone originally retrieved from the Woustwiller quarry, in Eastern France. The mineral composition and micro-structural characterization of this sedimentary rock, reported here in Table 1, were documented by Bésuelle et al. [18] in an earlier experimental study on this particular porous sandstone. The initial porosity for each of the retrieved sample has been measured at 21% $\pm$ 1, showing a satisfactory consistency between sampling locations of the block.

The prismatic samples, of approximate size $50 \times 30 \times 25$ mm^3, are prepared as to have symmetric boundary conditions on opposite surfaces of the geometry by performing successive iterations of machining, polishing and later applying watercolor paint coatings. The allowable tolerance on the parallelism is $\pm$ 0.02 mm for each pair of surfaces in contact with the hard platens (hardened steel in direction 1 and sapphire glass in direction 2) and $\pm$0.03mm for the pair of surfaces in contact with the urethane membrane, after the strain gauge installation. The surfaces in contact with the platens are finally lubricated using a thin coating of a stearic acid and vaseline mixture, effectively minimizing end friction effects under high confining pressures [19]. This thin lubricant coating being translucide, the visual aspect of the fine speckle pattern applied over the surface is maintained after an homogeneous contact is established between the sample and the sapphire glass.

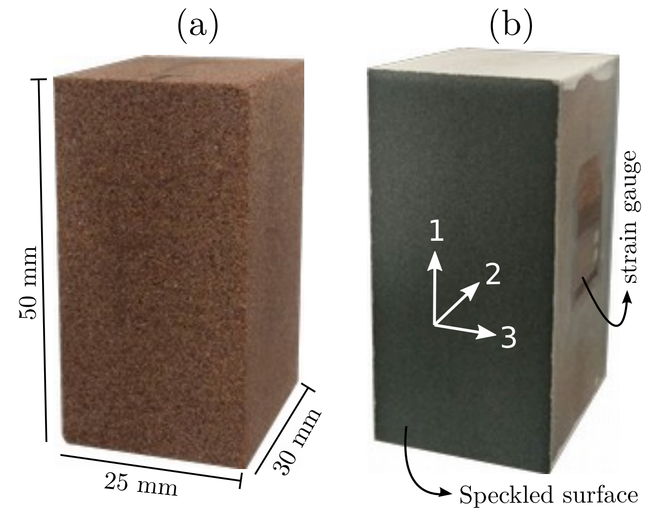

Figure 3: Intact prismatic samples of Vosges sandstone showing (a) the natural porous surfaces and (b) prepared surfaces with horizontal strain gauges, painted surfaces and the monochromatic speckle. Orthogonal vectors mark the spatial directions associated with the principal stress space.

2.4. Instrumentation and measurements

The unique conception of the TTA used in this study enables the monitoring of full-field surface kinematics, using digital image correlation (DIC), from photographs of one of the sample surface during the loading phase. The out-of-plane strains are also measured directly on the sample surface using strain gauge instrumentation.

The full-field photographs of the sample surface are captured through a sapphire viewport, oriented in the 1-3 plane (orientation as in Figure 3). The digital imaging system, a single-lens reflex (DSLR) 36 Mpx Nikon D800E camera, provides a spatial pixel size of 7 microns over the entire surface of the sample. In the camera configuration used to minimize noise and shutter vibrations, photographs were taken at regular intervals with a minimum time period of 3 seconds/image.

On the white painted and polished visible surface of the sample, a fine monochromatic speckle pattern is applied by paint atomization, using a precision airbrush, to create a random deposition of black watercolor droplets over the whole region of interest (ROI) (Figure 3b). This process enhances the optical texture and uniqueness of local zones of interest (ZOI) from the natural texture created by the surface heterogeneity on the surface of the porous sandstone. The DIC algorithm relies on the conservation of optical flow during the deformation process. Therefore, the spatial resolution, convergence and systematic error in the process rely on the quality of the optical texture in each ZOI. The texture quality is assessed for each created speckles by computing the autocorrelation function [20]. The autocorrelation radius is a scalar measurement of the pixel displacement where the autocorrelation function of a ZOI reduces by half, indicating the level of self similarity of the texture around this area [21, 22]. Measurements of the autocorrelation radius in the vertical and horizontal directions are shown in Figure 4a and 4b respectively for a typical surface ROI. For DIC, a speckle pattern with an autocorrelation radius of around 2 pixels is considered to provide an optimal texture quality which is independent of the acquisition noise.

The DIC algorithm used to performed the image analysis is the open source Software for Practical Analysis of Materials (Spam) developed as a collaborative and open source project [23]. The correlation algorithm, designed for 2D and 3D analysis, is based on a two step approach: an initial correlation to the nearest pixel, generating an approximation of the deformation field by tracking large rigid body motions, and subsequent iterations consisting in a sub-pixel correlation based on the initial approximation obtained from the first step. This latter operation allows for all possible affine (six degrees of freedom in 2D) transformations of the ZOI, to accurately track the local displacement at each node. One of the purposes of the displacement field obtained from DIC is to apply corrections to the sample's boundary displacement in the 1-3 visible plane, providing accurate global strain measurements. The strain in the horizontal direction 3 is computed from the horizontal displacement of DIC points at the two vertical boundaries. In the vertical direction 1, the external LVDT measurement is corrected at regular intervals using accurate DIC measurements, compensating deformation artifacts from the compliance of different parts of the apparatus (loading cell, surface contact interfaces) measured externally. The contribution of in-plane deformation to the global volumetric deformation of the sample is calculated from the sum of averaged outward displacements at each boundary. This

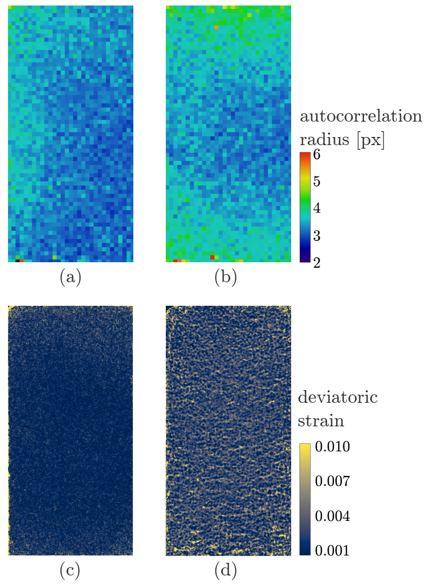

Figure 4: Assessment of speckle quality and measurement error in sample G16, at $\sigma_m = 60$ MPa and $\theta = 0°$, showing: the fields of autocorrelation radii in the vertical (a) and horizontal (b) direction, and image correlation of two photographs in the same deformation state (c), compared to the increment 1-2 reported in Figure 7.

method is equivalent to the computation of the contour integral for small deformation gradients.

Additionally, the two-dimensional fields of incremental local strain, calculated from the spatial first order derivative of the displacement field, are of clear interest in identifying localization patterns and their evolution. Nonetheless, due to reduced continuity compared to the discrete displacement field, the local strain field is more sensitive to the errors in the image acquisition process and selected DIC parameters (acquisition noise, choice of ZOI size, convergence error resulting from the DIC process). It is thus necessary to apply local corrections and filtering of the displacement field to obtain a better representation of the derived strain field. First, the field of correlation residuals, quantifying the correlation error and non-linear deformation, is used to mask the displacement field; the values at poorly correlated nodes are replaced by a weighted interpolation of surrounding converged nodes. Second, a sequential median and mean convolution of the nearest neighbors is performed to render a continuous field by eliminating isolated singularities, at the expense of degrading the local pixel-scale deformation measurements.

From the resulting filtered displacement field, a local strain tensor is calculated based on the displacement of 4 neighboring nodes using a regular grid layout and linear finite element shape function interpolations. This procedure yields a spatial map of the local deformation gradient tensor at the center of each cell. Since large rotations and strains may develop locally, large transformation formalism is used for the local deformations derived from the incremental displacement field (see Appendix A).

To assess the effect of acquisition and correlation errors on the strain measurements, Figure 4c shows a deviatoric strain field calculated using two photographs acquired in the same deformation state, at the beginning of the deviatoric loading phase (at photograph 1). In the deformation range of interest, the strain measurement error is seen to be only slightly more important in regions of the sample surface where the the autocorrelation radius is higher. However, this error remains negligible in comparison to the magnitude of localized deformation observed in selected subsequent increments of the deviatoric loading phase (increment 1-2 is illustrated in Figure 4d for comparison).

To measure the out-of-plane deformation in direction 2, strain gauges were installed horizontally at mid-height on both sides of the sample surfaces in contact with the soft membrane. For the axisymmetric compression experiments, where $\sigma_2 = \sigma_3$, it was observed that strain gauges in direction 2 and DIC measurements in direction 3 were in good agreement until pronounced localization effects start to develop. This reveals a good correspondence between different measuring techniques as well as strain homogeneity despite different types of boundary conditions with different end-friction and possible bulging effects developing in independent directions 2 and 3. The global volumetric strain is represented as to take into account the full three dimensional in-plane and out-of-plane components in each of the three principal strain directions.

3. Experimental Results

Guided by the study of Bésuelle et al. [18] in which axisymmetric compression (ASC) and extension (ASE) loading experiments were performed on samples of the Vosges sandstone (extracted from the same initial block), the range of mean stress was selected to investigate deformation mechanisms associated with the brittle-ductile transition regime. The present experimental campaign thus consisted of ten monotonic loading experiments following

Table 2: Summary of stress states and angle β at $\tau_{oct}^{peak[1]}$ for each of the 10 loading paths

σ_m^{peak} [MPa]	θ^{peak} [°]	$-\sigma_1^{peak}$ [MPa]	$-\sigma_2^{peak}$ [MPa]	$-\sigma_3^{peak}$ [MPa]	τ_{oct}^{peak} [MPa]	β [°]
61.1	0.0	128.7	27.2	27.3	47.8	50
61.7	16.0	121.0	46.8	17.3	43.6	56
62.3	29.6	110.6	61.9	14.5	39.3	61
61.9	45.4	96.9	75.1	13.7	35.2	64
62.0	59.9	87.9	87.8	10.4	36.5	64
90.0	0.0	169.0	50.4	50.4	55.9	43
90.1	15.1	166.4	69.8	34.0	55.9	47
90.0[2]	14.9[2]	168.7	68.9	32.6	57.5	-
91.4	32.4	148.8	94.2	31.2	48.1	54
90.0	44.9	136.9	107.1	26.2	46.8	56
89.9	59.9	122.8	122.7	24.1	46.5	56

[1] The *peak* superscript designates the moment when the octahedral stress reaches its maximum value.

[2] Duplicated experiment at σ_m=90 MPa and θ=15° not represented in subsequent Figures.

invariant controlled loading paths at five prescribed Lode angles (0, 15, 30, 45 and 60°) at two mean stresses (60 and 90 MPa).

A summary of the peak principal stresses and corresponding stress invariants is presented in Table 2. In this Table, a duplicated data point at σ_m=90 MPa and θ=15° is provided. Since only the stress values for this additional experiment are available, it is not represented in subsequent Figures, but helps to consolidate the result for this loading path. Due to differences in the correction terms applied to Equation 2, embedded in the servo-controlled loading program (constant for tests at σ_m = 60 MPa; linear dependency with σ_3 for tests at σ_m = 90 MPa) and in the post-experimental correction functions (linear dependency with σ_3 for all tests), there is a slight discrepancy between the mean stress and Lode angle initially prescribed and the peak values of the controlled invariants reported in Table 2. The importance of the correction terms dependence on the cell pressure (σ_3) was only assessed after the first part of the experimental campaign. The deviation is however not significant compared to the mean stress and Lode angle intervals between the different selected stress paths. Therefore, the closest prescribed values will be used to reference the different loading paths.

3.1. Mechanical response

The evolution of global octahedral stress (τ_{oct}) and volumetric strain (ϵ_{vol}) during the deviatoric loading phase is reported for each experiment against the octahedral strain (γ_{oct}) in Figure 5. A first comparison of the different mechanical responses at the two studied mean stresses indicates that, irrespective of the Lode angle prescribed for each experiment, an increase in the mean stress, from 60 MPa to 90 MPa, favours a slower bending of the octahedral stress versus strain curve during the pre-peak regime, while the initial stiffness is essentially the same. Consequently, the peak octahedral stress is found to increase with the mean stress, a classical result often reported in the literature for experiments following ASC loading paths. While the increase in the peak stress with the mean stress is more pronounced at a Lode angle of 15°, the variation in this increase with the Lode angle remains moderate and appears to become relatively constant between experiments at higher Lode angles of 30° to 60° (Figure 6).

At each of the two investigated mean stresses, loading paths following different Lode angles in the octahedral plane also promote a significant variation in the mechanical response during the late pre-peak regime. During this stage of loading, the octahedral stress level along the stress-strain curves is consistently lower at higher Lode angles. A noticeable difference in the stress-strain response is also apparent between the lower (0°, 15°) and higher (30°, 45°, 60°) values of the Lode angle (mostly apparent at σ_m =90 MPa). This marked difference in the octahedral stress evolution during the pre-peak regime results in a consistent decrease in the peak octahedral stress with increasing Lode angle, while the octahedral strain corresponding to the peak stress tends to increase. Between the two prescribed mean stresses, this influence of the Lode angle on the peak stress occurs over a different range of Lode angles. In Figure 6a, it is seen to steadily decrease from 0 to 45° at σ_m=60 MPa and over a shorter range of 15° to 30° at σ_m=90 MPa (consolidated by the additional data point in Table 2). The non-linearity in the peak octahedral stress transition indicates an evolution of the shape of the failure surface with both the mean stress and the Lode angle (Figure 6b). Furthermore, the variation in the peak octahedral stress over the full range of Lode angles, from 0° to 60°, is of comparable magnitude to the effect of the mean stress for the range investigated in the present study (from 60 to 90 MPa). As for the residual stress, after peaking and softening, the values depend on the mean stress and are rather independent of the Lode angle, except for the tests at 0° angle where the residual stress is clearly above the

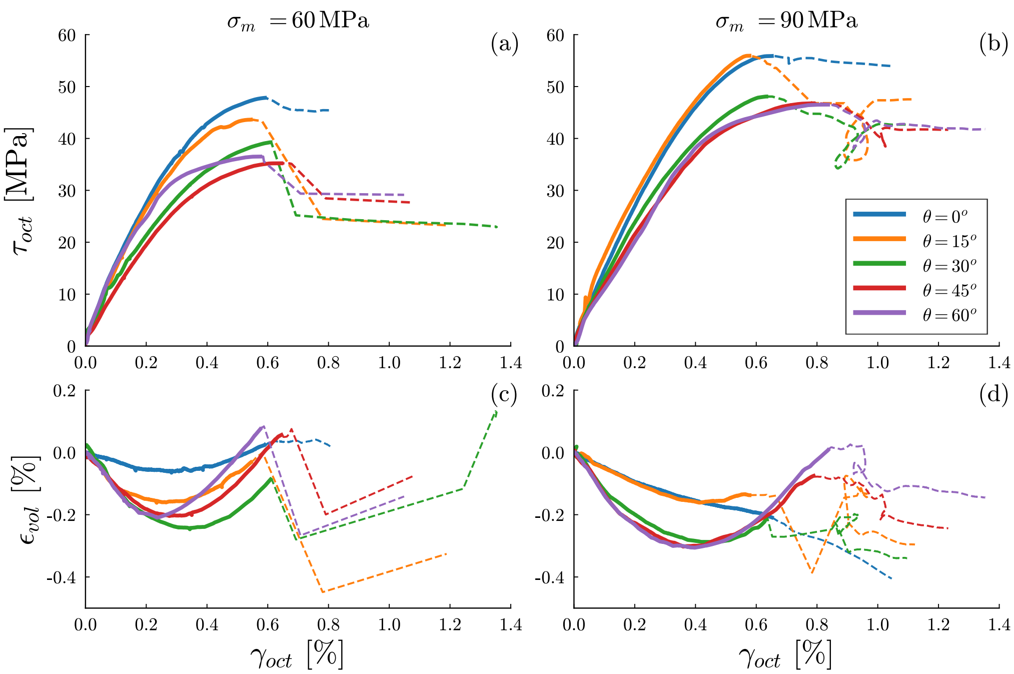

Figure 5: Octahedral stress (τ_{oct}) and volumetric strain (ϵ_{vol}) as a function of octahedral shear strain (γ_{oct}), analogue to τ_{oct} in the strain space. The curves are dashed in the post peak regime, indicating a loss of quasi-static conditions and apparatus displacement control regulation in all but tests at a Lode angle of 0°.

other values.

The evolution of global volumetric deformation, combining measurements using DIC in the 1-3 plane and strain gauges in the out-of-plane direction 2, is also affected by the prescribed mean stress and Lode angle. In this particular case, for selected loading paths at constant mean stresses, it can be noted that the elastic part of the volumetric deformation is theoretically vanishing. Therefore, the initial compactant behavior, represented in Figure 5c-d, suggests an inelastic deformation is occurring at the initiation of the deviatoric loading phase. At the mean stress of 60 MPa, all samples displaying an initially compactant behavior transition into a dilatant phase at approximately halfway through the pre-peak phase. At this lower mean stress, a distinctly lower volumetric change is observed for the Lode angle of 0°. In comparison, the samples tested at higher Lode angles display both a more pronounced initial compactant and a subsequent well defined dilatant phase.

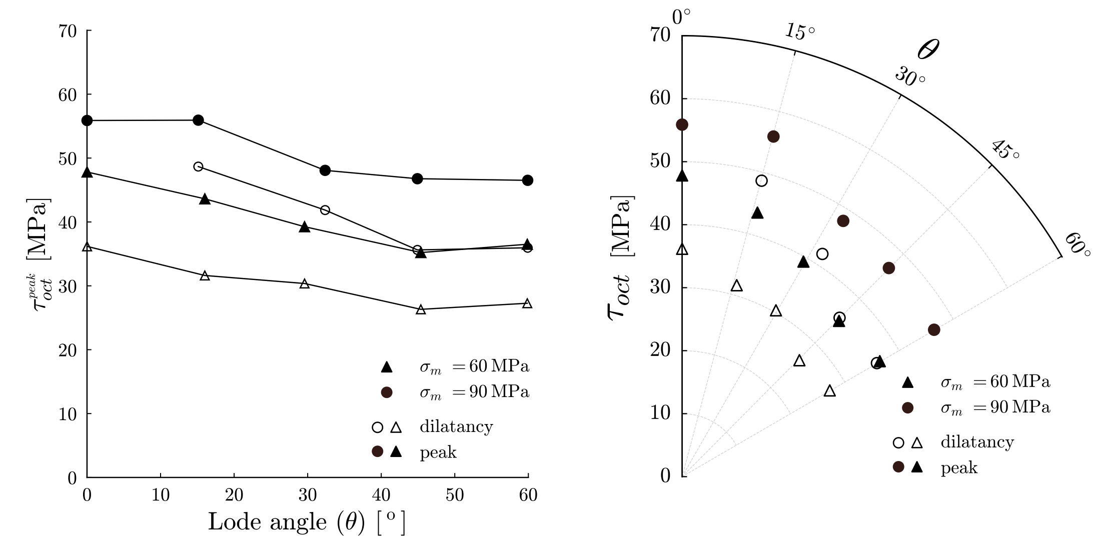

(a) (b)

Figure 6: Evolution of the octahedral stress at dilatancy (τ_{oct}^{dilat}) and peak stress (τ_{oct}^{peak}) in (a). The same dataset is represented in the octahedral plane in (b).

At the mean stress of 90 MPa, the volumetric deformation, for the different loading paths, follows two distinct evolutions during the pre-peak regime: at the lower Lode angles of 0° and 15°, a monotonic volumetric deformation sustains a moderately compactant behavior of the samples (however, a very slight dilatation is observed at 15° towards the stress peak); whereas, at the higher Lode angles, the response is similar to the behavior observed at the lower mean stress, displaying a more pronounced compactancy followed by a well defined dilatant phase. It is possible to identify the octahedral stress at the octahedral strain where the inception of dilatancy occurs for each loading path. In Figure 6, the decrease in the octahedral stress at dilatancy with decreasing mean stress and increasing Lode angle is concordant with the trend in the transition of the peak octahedral stress. In this Figure, the value at $\sigma_m = 90$ MPa and $\theta = 0°$ is omitted since the volumetric deformation is continuously compactant for this loading path. At the higher mean stress and intermediate values of the Lode angle, the difference between the octahedral stress at dilatancy and at the peak decreases with decreasing Lode angle, while it remains relatively constant for all Lode angles at the lower mean stress.

In the post-peak regime, all samples tested at a mean stress of 90 MPa have a compactant total volume strain past their respective peak octahedral stress. However, since mature localization structures tend to emerge around the peak stress, global measurements from average boundary displacements become discontinuous in this phase of the mechanical response. The global strain measurements are therefore less representative of the predominant deformation mechanism occurring inside the sample. In addition to being the dominant deformation mechanism at the sample scale during the post-peak regime, localized deformations also play an important role on the mechanical response during the pre-peak regime. In the next section, incremental full-field measurements are presented and compared for the different loading paths, enabling to characterize the emergence of precursors and early deformation structures during the pre-peak regime, and their relation to the development of highly localized structures near and past the peak stress.

3.2. Localization patterns

A full-field representation of local deformation, obtained from DIC in the 1-3, plane enables the identification of strain localization structures developing during the deviatoric loading phase. In the multi-page Figure 7, incremental 2D deviatoric and volumetric strain fields for each of the 10 experiments are depicted in consecutive series, from photograph $n \rightarrow n+1$. Each increment in the series, associated with each experiment at different loading paths, represents different characteristic phases of the mechanical and kinematic behavior: an early quasi-linear phase (1-2), an intermediate phase of volumetric compaction (2-3), the inception of dilatancy generally associated with the inception of early deformation bands (3-4), the intensification of localized zones into well developed early deformation bands (4-5), the development of mature localization structures organized into a single or multiple parallel and conjugated bands (5-6), brittle faulting or propagation of mature deformation band(s) (6-7). The series of photographs, from which the represented incremental strain fields are produced, are labeled on the associated individual stress-strain and volumetric curves.

In the initial volumetric compaction phase represented in increment 1-2, the deviatoric strain fields for all loading paths show relatively similar patterns of weakly defined regions of higher strain deformation. During this early loading phase, the deviatoric strain fields thus present some identifiable heterogeneities at the finer scale, where a spatial variation in the deformation is noticeable between neighboring correlation points forming small distributed clusters. Nonetheless, the represented strain fields do not, at this stage, exhibit any strong evidence of localization clustering or organization at the sample scale.

In full-field images of subsequent increments, following photograph 2 in respective experiments, two distinct types of deformation bands can be identified to sequentially emerge into well defined localization structures. The first type, referred to as *early deformation bands*, is observed to emerge well before the peak stress and develop in series of parallel and conjugated linear clusters of limited length, visible mostly in the central section of the ROI. The localization structures which are well defined in increments 3-4 and 4-5, can also be observed, if one looks closely, as weak precursors in increment 2-3. The second type, referred to as *mature deformation bands*, later develop close to the peak stress and is characterized by one or multiple extended localized regions traversing across the sample. Mature deformation bands can be seen to initiate during increment 4-5 and 5-6, and to fully develop during increments 5-6 and 6-7 in respective experiments.

The early deformation bands are seen to emerge from a progressive clustering of strain localization in specific areas of the visible surface of the samples, forming preferentially orientated linear structures which are continuously evolving throughout the later pre-peak regime. During this phase, the deviatoric strain inside early deformation bands gradually intensifies and further localizes in specific regions of the ROI. This evolutive behavior forming localized regions is most noticeable for experiments following loading paths at the higher mean stress of 90 MPa and higher Lode angles. It is also during increments 3-4 and 4-5, following the inception of the incremental global dilatancy, that the volumetric strain fields start to show significant localized dilatant zones, preferentially organized where localization structures are also, and more noticeably, observed in the deviatoric strain fields. It is therefore worth noting that, even for a relatively high porosity sandstone, the early deformation bands are dilatant except for low Lode angles.

For all studied loading paths, the continuous evolution of strain localization towards the end of the pre-peak regime leads to the formation of mature deformation bands, which develop concurrently to rapid stiffness weakening effects and a well defined transition of the mechanical response from a pre-peak to a post-peak regime. The development of these mature bands tends to occur in regions of the visible surface where early deformation bands have been persistent during the late pre-peak regime. After the peak stress, during increments 5-6 and 6-7 of Figure 7, most loading paths are seen to promote

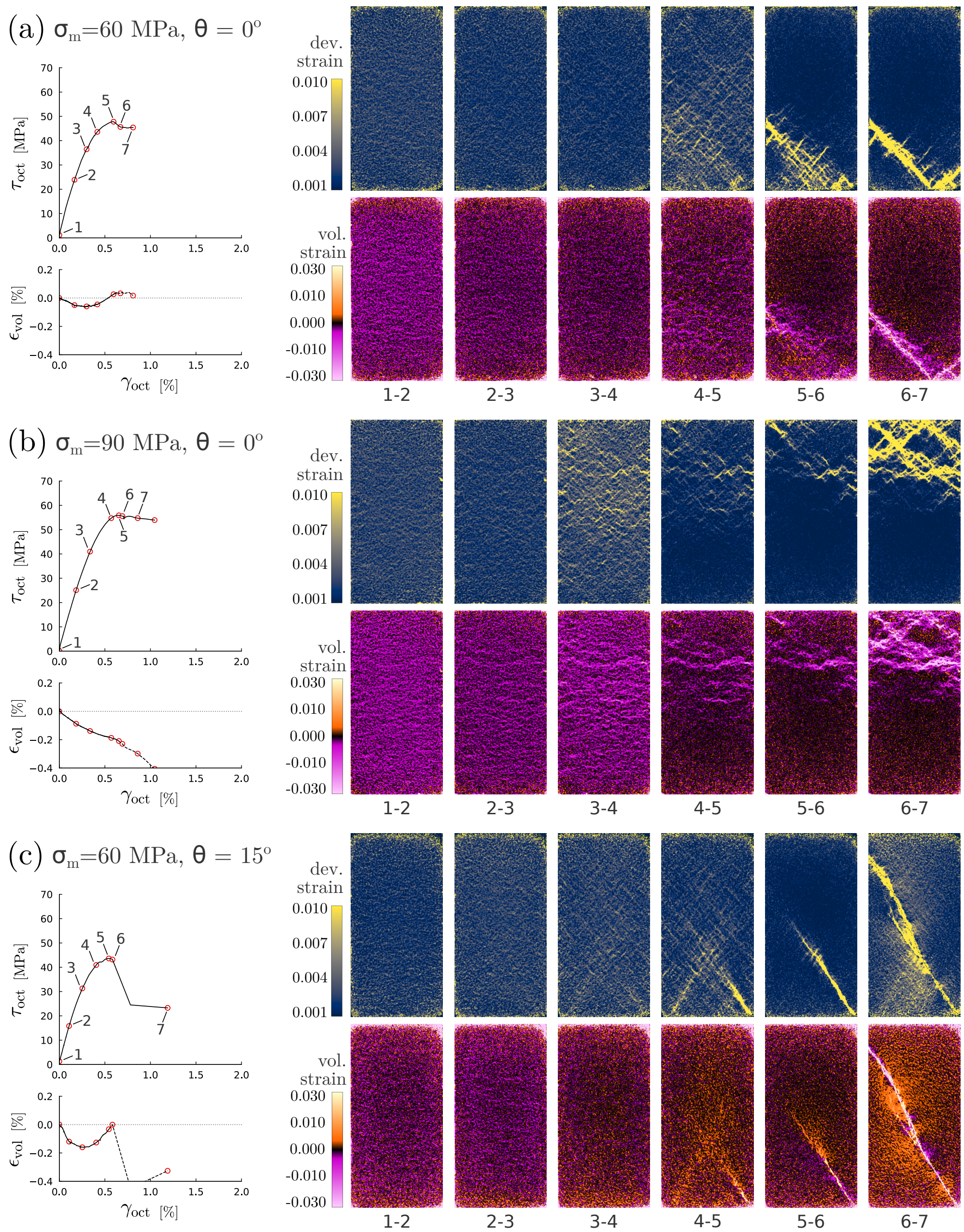

Figure 7: (part 1) Evolution of deviatoric and volumetric strain fields over the 2D ROI, for selected consecutive loading increments. The stress state and 3D volumetric deformation corresponding to each photograph are identified on the macroscopic curves by red circles.

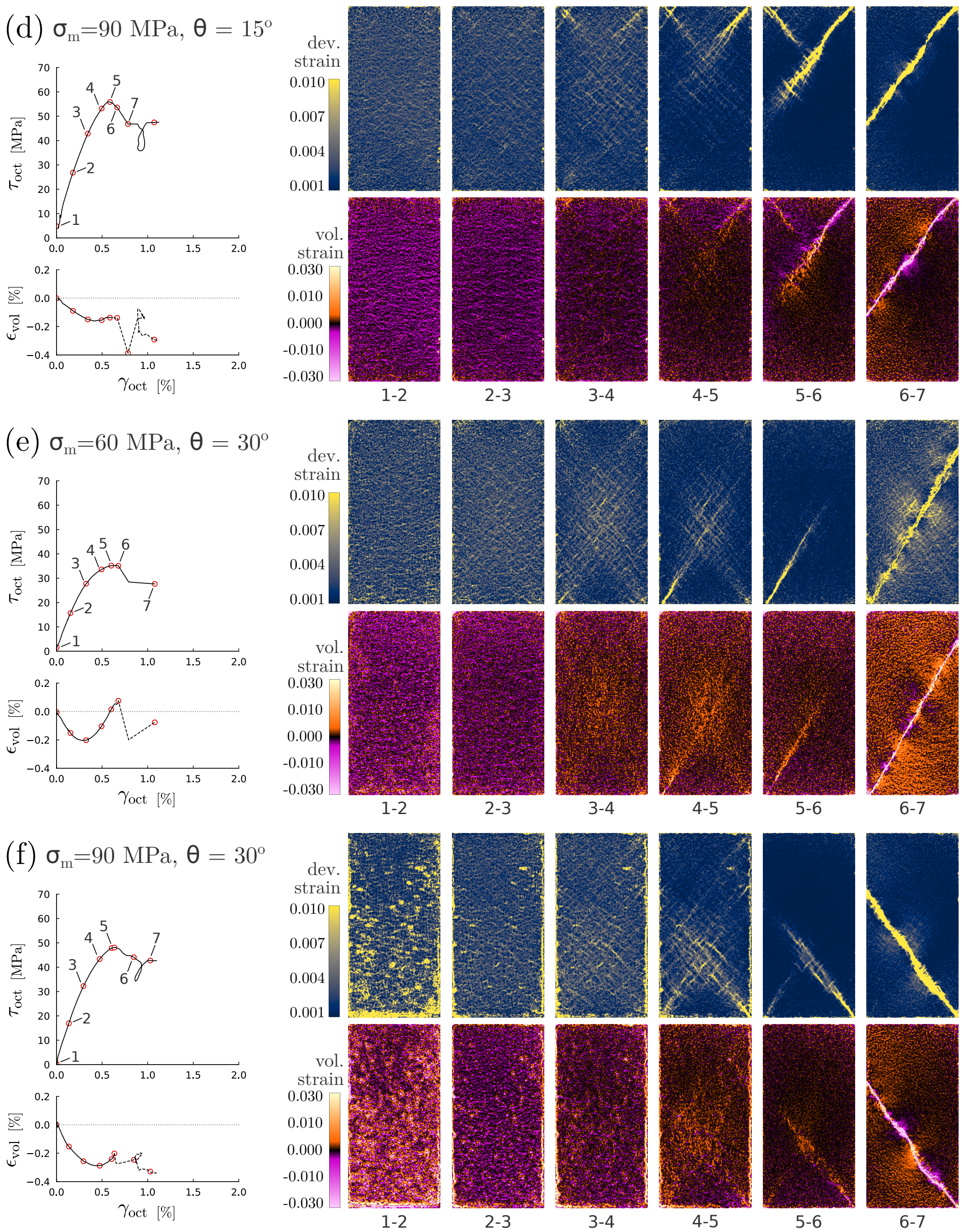

Figure 7: (part 2) Evolution of deviatoric and volumetric strain fields over the 2D ROI, for selected consecutive loading increments. The stress state and 3D volumetric deformation corresponding to each photograph are identified on the macroscopic curves by red circles.

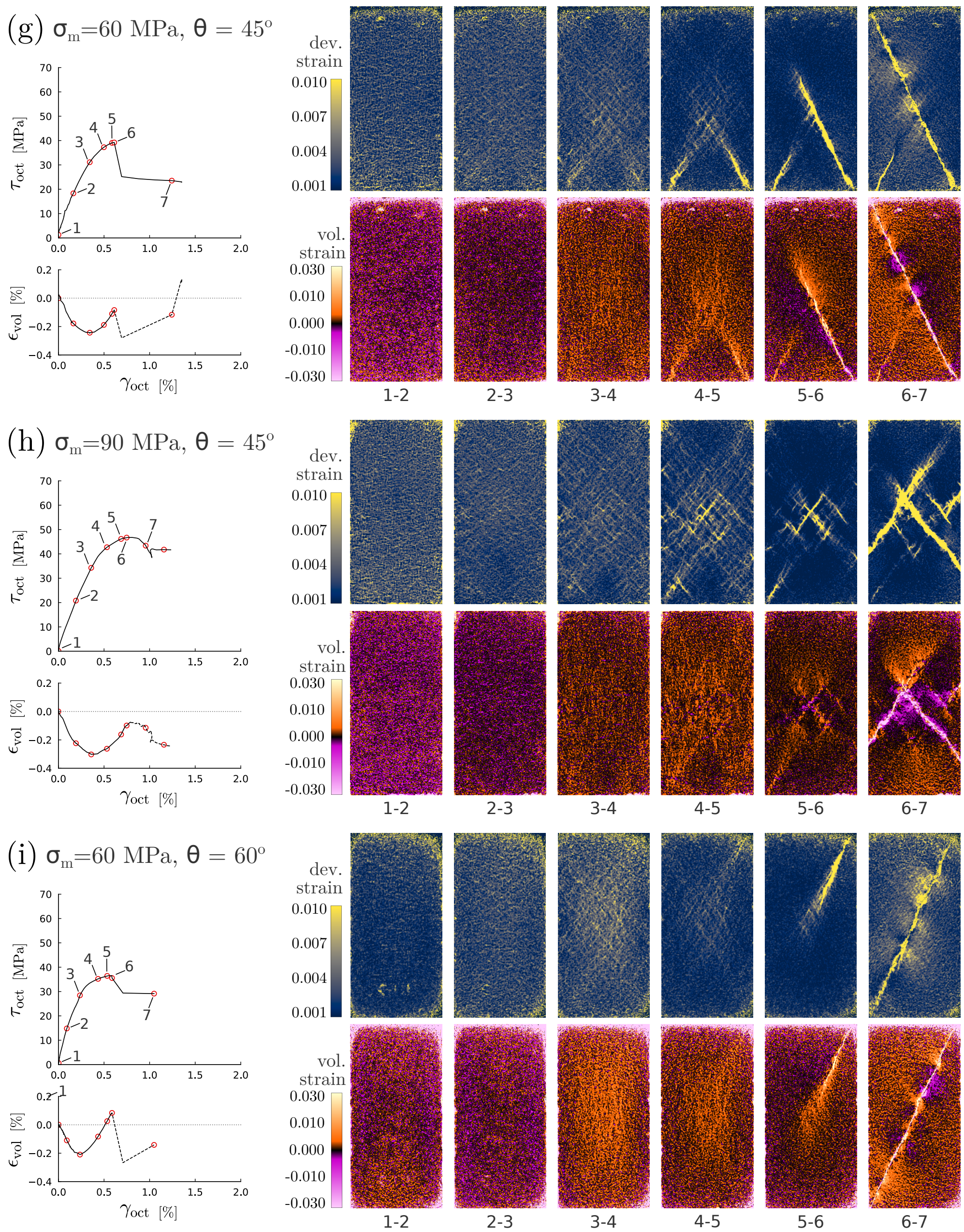

Figure 7: (part 3) Evolution of deviatoric and volumetric strain fields over the 2D ROI, for selected consecutive loading increments. The stress state and 3D volumetric deformation corresponding to each photograph are identified on the macroscopic curves by red circles.

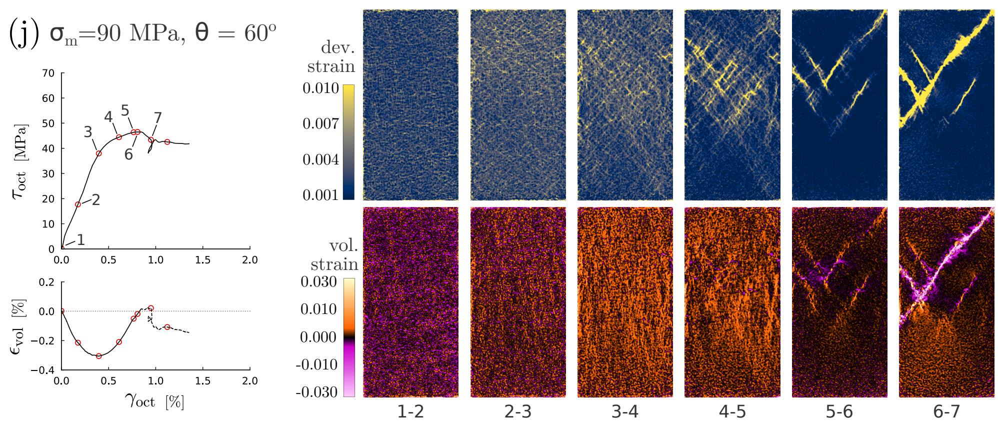

Figure 7: (part 4) Evolution of deviatoric and volumetric strain fields over the 2D ROI, for selected consecutive loading increments. The stress state and 3D volumetric deformation corresponding to each photograph are identified on the macroscopic curves by red circles.

a rapid concentration of strain localization into a unique linear structure propagating through the sample. Once such a well developed localized region starts to form, it tends to attract additional deformation. A notable exception to this deformation mode is identified for the loading path in Figure 7b (at $\sigma_m = 90$ MPa and $\theta = 0°$), where mature deformation bands are continuously activated and seen to relocate during the post-peak regime.

For samples tested at a mean stress of 60 MPa and a Lode angle greater than 0°, the development of mature deformation bands ultimately results in a global mechanical instability just after the peak stress, which can be explained by the relatively low stiffness of the apparatus compared to the absolute value of the tangential stiffness of the samples during the post-peak regime. Under these conditions, the deformation band propagates quasi-statically approximately halfway through the sample before quasi-static conditions are lost. At this instant, a complete propagation of the localized zone occurs dynamically, as elastic strain energy accumulated in both the sample and the apparatus, is suddenly released. For this type of failure mechanism, the resulting deformation zone is mostly concentrated around a unique and narrow band, with a normal of the band oriented at a moderately high angle (45° to 65°) with respect to the most compressive principal stress.

At the higher mean stress of 90 MPa and Lode angles greater than 0°, while mechanical instability can occur (see pressure regulation loops in Figure 5), the softening response is generally better controlled. At this higher mean stress level, a number of localized structures evolving from early deformation bands are more prone to coalesce and form a complex localized zone during the inception of a mature deformation band. The outcome of this coalescence process is a higher variability in the band thickness and internal orientation, which is not entirely captured by a single characteristic length. In increment 6-7 of Figure 7, a combination of compactant and dilatant zones is observed around the mature deformation band, corresponding to alternating localization orientation along the deformation band.

A substantial difference in the manifestation of mature deformation bands is observed, at both mean stresses, for a Lode angle of 0°. For these particular ASC loading paths, it can be noted that the deformation bands are not necessarily polarized in the 1-3 visible plane since the minor and intermediate principal stresses are equal. In the presented strain fields, the mature deformation bands evolve through the continuous intensification of extended localized regions close to the peak stress and later in the softening regime. This mode of localization occurs under a systematically compactant volumetric strain of the mature deformation bands. Additionally, at the mean stress of 90 MPa, localized deformation regions evolve with the activation (and deactivation) of conjugated and parallel bands during the post-peak regime, resulting in a continuous relocation of the localized regions.

It is noted that in the majority of cases, but not in all, the mature bands pass through one of the corners of the sample. This corner attraction effect is well known in axisymmetric tests on cylindrical samples. However, the field measurements presented here clearly show that, probably thanks to the quality of the lubrication and the flatness of the surfaces, the deformations prior to the mature localization do not present any particular characteristics linked to the edges or corners of the samples. These appear to have a negligible impact on the overall response of the sample but sufficient to influence the position of the mature bands (not their orientation).

3.3. Deformation band angles and dilatancy angle

The orientation of early deformation bands ($\beta*$) and mature deformation bands (β) in the visible plane is measured as the angle between the normal vector to the quasi-linear localized regions and the direction of the most compressive principal stress (σ_1). By characterising the deformation band angles during the loading phase from the incremental strain fields, the measure of the band angles reflects the intrinsic response of the material

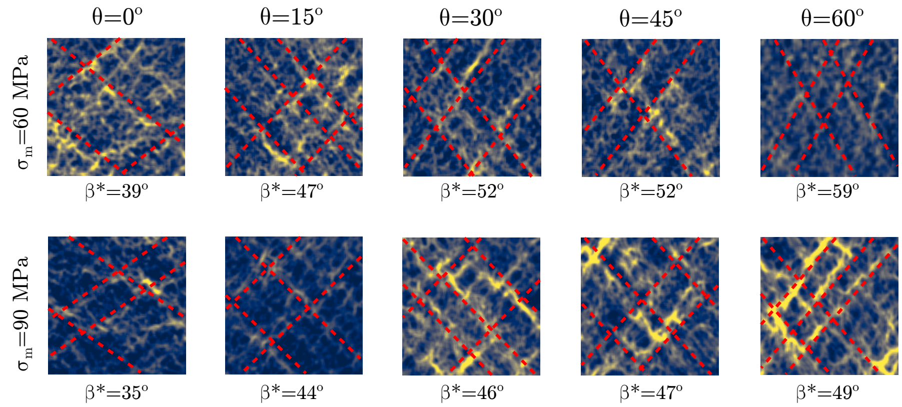

Figure 8: Identification of early deformation band angles (β^*) from deviatoric strain field increments.

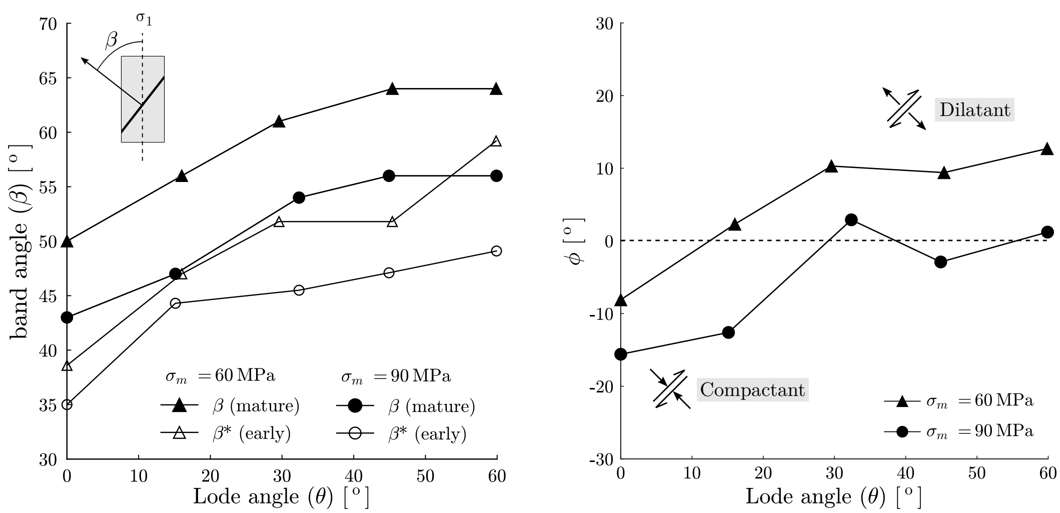

Figure 9: Evolution of the early and mature deformation band angles for the different loading paths in the octahedral plane(a), and dilatancy angle of mature deformation bands measured at their inception (b).

at the inception of the localized zones. Therefore, subsequent structural effects influencing the final band orientation, such as attraction to conjugated bands or boundary imperfections during propagation, can be avoided. This direct interpretation of the band angle at its inception is usually lost during a post-mortem assessment of the failed material.

The predominant angle β^* characterizing early deformation bands is qualitatively assessed for the series of parallel and conjugated bands observed in the central sub-region of the ROI represented in Figure 8. While a certain variability in the early band angles in each sample can be observed, the angle of the red lines represents the general orientation of these bands as they emerge in samples subjected to the different loading paths.

The measured angle of early and mature deformation bands is reported for each experiment in Figure 9a. In both cases, the angle is seen to increase with decreasing mean stress and increasing Lode angle. At both mean stresses, the change in deformation band angle is generally more pronounced at lower Lode angles and tends to become constant at the higher Lode angles. The mature deformation bands are also systematically developing at a higher angle than the preceding early deformation bands, regardless of the loading path.

The dilatancy angle of mature deformation bands is defined as

$$\tan\phi = \frac{\Delta D^v}{\Delta D^s} \ , \tag{3}$$

where ΔD^v and ΔD^s are respectively the volumetric and shear offsets across the localized region [24]. With large measurement errors due to the speckle quality degradation inside the highly deformed bands, the volume and shear offsets are obtained from the averaged displacement on each side of the band during increment 5-6. In Figure 9b the dilatancy angle, positive for a dilatant band, is seen to increase with decreasing mean stress and increasing Lode angle, in a trend that is comparable to the evolution of the mature deformation band angle. Therefore, experiments at a low Lode angle show a shear localization with compaction (compacting shear band) and at a high Lode angle, a shear localization with dilation (dilatant shear band). Nevertheless, in this simplified representation, the complexities observed in the mature deformation bands are not captured and must be kept in mind. This is particularly illustrated at the high mean stress of 90 MPa, where there are fluctuations in local orientations that impart a kind of roughness to the mature bands, as well as variability in volumetric strain along the band associated with this roughness.

4. Discussion

Experimental results from this campaign on a high porosity sandstone provide strong evidences that distinct loading paths, following deviatoric stress increments in the octahedral plane, promote substantially different mechanical and kinematic responses. The influence of the mean stress on the stress-strain behavior and failure mechanism, widely recognized in the case of axisymmetric (compression and extension) stress paths, is here also observed at intermediate values of the Lode angles. The effect of the different loading paths is also evidenced by the local strain evolution measured from full-field DIC. The significance of localization precursors, their evolution leading to different failure mechanism and the transition in the brittle to ductile regime is here further discussed.

4.1. Localization Participation Ratio

To compare the rich information conveyed by the spatial distribution of local strain measurements across different experiments, and quantify its evolution during loading, the Localization Participation Ratio (LPR), first introduced to the field of geomechanics by [25], is calculated for each series of increments. This scalar index of localization provides an appreciation of the deviatoric strain concentration over the visible plane. It is mathematically defined as

$$\mathrm{LPR} = \frac{1}{N_p} \frac{\left[\sum \epsilon_{dev}\right]^2}{\sum \left[\epsilon_{dev}^2\right]}, \tag{4}$$

where ϵ_{dev} is the spatially distributed local deviatoric strain (as defined in Appendix A), and N_p is the number of sampling points over the ROI. It is calculated for each incremental field of deviatoric strain, quantifying a departure from a homogeneous spatial distribution. Therefore, calculated values of the LPR are independent from the size of the selected increment, considering an equivalent homogeneous distribution of deviatoric deformation in this increment is above the noise level resulting from the image acquisition and treatment process. The upper limit, $LPR = 1$, corresponds to an homogeneous distribution of the considered spatial variable; whereas the lower limit depends on the number of measurements on the domain for which a strongly localized state (e.g. a Dirac distribution) results in $LPR = \frac{1}{N_p}$. The ROI over the considered two dimensional plane is a 600×300 area, excluding subregions on the fringe of the sample surface where the autocorrelation radius or DIC residuals were showing larger uncertainties.

Figure 10 shows the evolution of the LPR for the incremental deviatoric strain fields reported in Figures 7. For all tested samples, the LPR indicates a weak variation in diffuse localization during the pre-peak regime until a

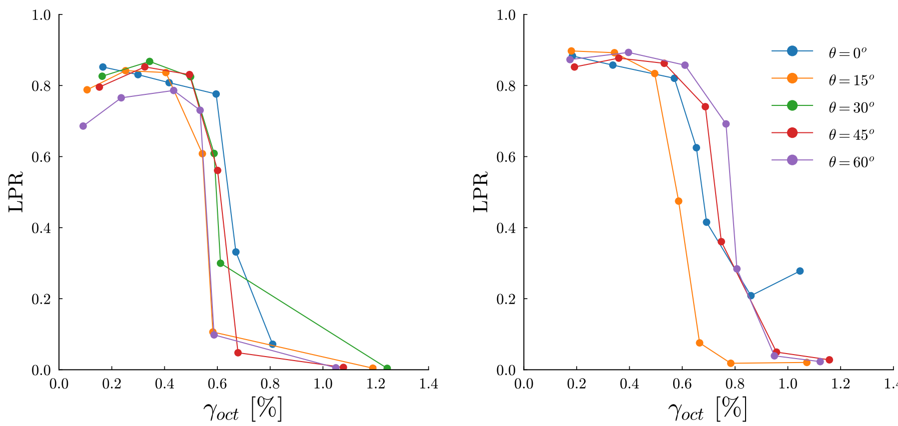

(a) σ_{m} = 60 MPa (b) σ_{m} = 90 MPa

Figure 10: Localization Participation Ratio (LPR) evolution with octahedral strain for tests at (a) σ_m=60 MPa and (b) σ_m=90 MPa . The position of each point correspond to the end of the interval in which the LPR is measured. The sequence of increments are labeled in one of the curve as a reference.

strong decrease is initiated during the increment 4-5 (near the peak-stress), characteristic of well-developed early deformation band and the inception of a mature deformation band. At the mean stress of 60 MPa, the LPR decreases rapidly at around 0.6% octahedral strain. At a mean stress of 90 MPa, for Lode angles of 0 and 15° the increase in the mean stress is seen to induce a decrease in the LPR at around the same octahedral strain of 0.6%. At higher Lode angles, the octahedral strain at which the LPR starts to decreases is however noticeably higher and shows a more progressive evolution towards the full development of mature deformation bands. Even if the spatial organization of deviatoric strain is not captured in the LPR, this observation is consistent with the progressive evolution in the coalescence of localized deformation at higher mean stress and for Lode angles above 15°. This dissimilar kinematic response to an increase in the mean stress, between Lode angles above and below 30°, suggests a strong influence of the Lode angle on the deformation regime leading to failure.

4.2. From localization precursors to failure

During the early deviatoric loading phase, corresponding to increments 1-2 and 2-3, the relatively large inelastic compaction observed at the sample scale for experiments conducted at higher Lode angles occurs in a relatively diffuse deformation process, which is reflected by the initially stable or slightly increasing LPR. Therefore, during this phase of loading, the sample deforms mostly in the absence of identifiable structural localization patterns. Nonetheless, samples experiencing a higher initial compaction at the sample scale, are associated with a subsequent well defined transition into a dilatant regime, during increment 3-4. Concurrently, these samples present a higher deviatoric strain intensity and dilatant volumetric strains concentrated inside early deformation bands. This relation between the initial compactant behavior and the later localization behavior at different Lode angle emphasizes the role of selected loading paths in a single octahedral plane in promoting different diffuse deformation responses and transitions into the development of localization structures.

The emergence of dilatant early deformation bands results from the progressive clustering and densification of initially scattered localization precursors. Under monotonic deviatoric loading conditions in the octahedral plane, the inception and intensification of these early bands appear to be driven by shear deformation with a predominantly dilatant behavior. In this instance, the dilatant volumetric strain, mostly apparent in localized zones at higher Lode angles, is concurrent with a reversal from an incremental compactancy to an incremental dilatancy in the global volumetric deformation measured at the sample scale. This observation suggests that the presence of dilatant early deformation bands constitute an important deformation mechanism contributing to inelastic deformation and a concentration of weakening deformation in fewer regions of the porous rock during the later pre-peak regime. The continued development of early deformation bands appears to be an important phenomenon concomitant with the loss of linearity in the octahedral stress-strain curve. It can therefore be inferred that, at least for the range of mean stress investigated here, the lower octahedral stress attained at higher Lode angles is related to the emergence and continuous organization of these early structural deformation zones developing well before the peak-stress.

In samples where a well defined dilatant regime is observed, i.e. for loading paths where $\theta > 0°$, strain localization tends to rapidly coalesce and concentrate into fewer localized regions of higher intensity and increasing dilatancy as the peak stress is approached. Consequently, during this process, previously localized regions tend to progressively become inactive. The peak stress is reached when a dominant sublinear zone of high strain concentration propagates through the sample and develops into a mature deformation band by connecting early deformation bands of limited length into a continuous structure. During this transition, a dilatant region, comprising earlier deformed regions, remains active ahead of the tip of the propagating mature deformation band (identified in Figure 11b-c). Since early deformation bands tend to initially form at a lower angle than the later mature deformation bands, the localized zones become connected by sections of alternating internal angles. Figure 11 illustrates the presence of echelon type patterns connecting early deformation bands of higher activity along the length of the mature localized region, with associated dilatant (high angle) and compactant (low angle) zones. The prevalence of this deformation mechanism is corroborated by similar, although post mortem, observations in [7]. In a series of experiments on Dunham dolomite in true triaxial loading conditions, the author identifies the existence of secondary micro cracks, here identified as early deformation bands, on the sample surface, as well as a variation in the internal angles of mature deformation bands along its length. Consequently, the formation of early deformation bands, here identified at a lower inclination, seems to plays a significant role on the roughness and thickness variation of mature deformation bands, which in turns can influence the post-failure behavior of the material, during the quasi-stable permanent regime. This suggests that the spatially inhomogeneous deformation and induced anisotropy from oriented early localized structures can influence the later occurring failure mode in the material.

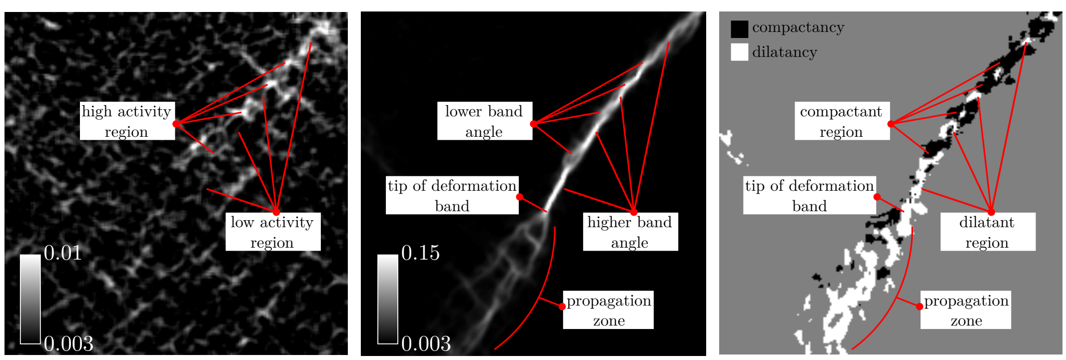

(a) deviatoric strain - pre-peak (b) deviatoric strain - peak (c) volumetric strain - peak

Figure 11: Correspondence between early localized regions (a) during the pre-peak and the mature deformation band angle variation (b) and volumetric strain (c) at the peak. The represented sub-regions are increments 3-4 (pre-peak) and 5-6 (peak) of Figure 7d.

While compactant sub-regions along propagating deformation bands are observed at higher Lode angles, a contrasting continuously compactant type of deformation bands is only observed in samples tested at a Lode angle of

0°. For these particular ASC loading paths, deformation mechanisms differ significantly in terms of the development of localization structures during the transition around the peak stress. In this case, strain localization appears to be more distributed across the sample and develops simultaneously in multiple and extended active regions. During the late pre-peak to post-peak transition, the distribution of compactant deformation bands over a larger part of the sample suggests that, unlike dilating deformation bands, compactant bands have a lesser tendency to concentrate strain localization into a single linear mature deformation band, as previously suggested by [18]. Instead, the stable deformation process inside compactant band result in a network of evolving and highly connected internal sub-structures. This phenomenon is most apparent at the higher mean stress of 90 MPa, where multiple localized regions remain active during the post-peak regime and progressively relocate to nearby lesser deformed regions of the sample.

4.3. Brittle-ductile transition

For the range of stress paths studied in this experimental campaign, the variation in the mean stress and Lode angle between different loading paths is shown to have a significant influence on the global mechanical response and on the spatial evolution of localization phenomena. For the studied Vosges sandstone, an increase in the mean stress or a decrease in the Lode angle systematically induce a transition from a brittle to a ductile mode of failure. This transition is apparent in the mechanical response by an increase in the maximum octahedral stress, a progressive softening in the post peak and a reduction in the incremental volumetric strain at the peak. In terms of localized deformation modes, the brittle to ductile transition is seen through a decrease in both the band angle of early and mature deformation bands and in the dilatancy angle measured at the peak stress. Furthermore, concentrated dilatant early and mature deformation bands are systematically observed in samples showing a brittle failure mode, while a compactant behavior and relocation of mature deformation bands is associated with a ductile failure mode.

The transition in the brittle-ductile behavior in the deviatoric plane is further evidenced by the non-linear shift in the peak octahedral stress occurring in the low to intermediate interval of Lode angles (Figure 6). The similarity in the peak value between 0° and 15° at the mean stress of 90 MPa, reinforced by an additional point at 15° (Table 2), emphasizes the observation of a shorter transition range at higher mean stress. Past this transition, further increase of the Lode angles appears to have a diminishing effect on the peak stress and mature deformation band angles.

In terms of strain localization patterns, a brittle-ductile transition can generally be associated with the aforementioned change in the type of deformation bands formed during the post-peak regime. A shift in the deformation patterns towards a ductile response is seen to occur with a decrease in the Lode angles. In a study following similar loading paths at imposed mean stress and Lode angle, Ingraham et al. [13] observed a similar trend, where a decrease in the Lode angle results in a shift from well defined narrow deformation bands to a more diffuse mode of failure, where individual bands could not be identified in a post-mortem assessment. The authors also noted that the shift towards a more ductile response occurs at higher mean stresses for higher Lode angles.

Despite a general concordance between the mechanical and kinematic (i.e. localization pattern) interpretation of the brittle-ductile transition, it can be noted that, for samples tested at a mean stress of 90 MPa and Lode angles of $0°$ and $15°$, while having a similar octahedral stress-strain response during the pre-peak regime and a close peak octahedral stress, their mature localization patterns is quit different. At the Lode angle of $0°$, a ductile (continuously relocating and compactant) deformation mode is observed, while at $15°$ the deformation band can be seen as more brittle (propagating and compactant with dilatant zones). Therefore, in this case the ductility in the deformation mode is not uniquely related to the macroscopic stress-strain response, but is specific to the loading path in the octahedral plane.

The range of the brittle-ductile transition is concurrent with a progressive shift in the intermediate principal strain (direction 2) with increasing Lode angle and the increasing dilatant behavior observed in early deformation bands. From these experimental observations, it appears that stress paths promoting a shortening of the sample in the intermediate principal direction 2 is contributing to localized dilatant effects in the visible plane (1-3). The concentration of this effect in early deformation bands implies that this mechanism probably exacerbates the alteration and weakening of the rock fabric in localized zones.

In loading paths promoting a transition towards a ductile failure, the total octahedral strain in the sample at the inception of the softening regime is equivalent or lower than for loading paths leading to a more brittle failure. Therefore, the higher peak octahedral stress attained in those experiments seems to be attributed to the slower bending in the stress strain response, rather than a capacity of the samples to sustain higher global deformation, as the mechanical response transitions toward the ductile regime.

5. Concluding remarks

The presented experimental study, investigating the mechanical behavior and full-field kinematics of a high porosity sandstone, contributes original results obtained under unconventional and rarely studied true triaxial loading paths in the octahedral plane. Using a unique experimental setup, strain localization structures and their evolution during the loading phase were assessed and compared for different deformation regimes. The use of optical images, acquired at a high spatial and temporal resolution, and analysed through digital image correlation (DIC), proved to be an effective method to explore the role of micro-kinematics on the inception of localization structures leading to different failure modes.

This study highlighted important transitions in the material response between the series of experiments performed at different purely deviatoric loading paths. Notably, it is demonstrated that an increase in the prescribed Lode angle results in a systematic increase in the angle of early (pre-peak) and mature (peak and post-peak) deformation bands, an increase in the dilatancy angle of mature deformation bands, as well as a decrease in the peak octahedral stress and an embrittlement of the sample response.

The evolution of kinematic structures identified at the surface of the sample during the pre-peak regime clearly showed the emergence and continuous development of early deformation bands. These bands are seen to organize into parallel and conjugated sublinear strain localization regions of limited length well before the peak stress. The ubiquitous presence of this inhomogeneous mode of deformation seems to play an important role in the development of inelastic and dilatant effects at the sample scale. Also, the observation of early strain localization is concordant with the continuous weakening of the rock fabric integrity during the pre-peak regime. During this loading phase, the progressive intensification and concentration of strain in early deformation bands culminate into the formation of either dilatant mature deformation bands propagating through the sample (fragile) or the continuous deactivation/relocation of larger localized regions during the softening regime (ductile). For the range of mean stresses investigated in this study, the brittle-ductile transition, observed in both the strain localization patterns and the mechanical behavior, occurs mostly in the lower to intermediate range of Lode angles, between $\theta = 0°$ and $30°$.

Finally, the angle of early deformation bands is found to be lower than the angle of mature deformation bands. Therefore, as early localized regions become connected, the alternating variation in internal angle of mature deformation bands influences their aspects (departure from flatness) and thus the material residual strength in the permanent regime.

These observations are important in taking into account the non-linear and complex response of porous rocks subjected to general true triaxial loading paths. Therefore, the relation between the mechanical response and development of strain localization, especially in the early stages of loading, should be considered to enrich existing constitutive models for high porosity sandstones, as well as other analog materials characterized by cohesive-granular micro-structures.

Appendix A. Strain decomposition

In the Software for Practical Analysis of Material, the deformation gradient tensor, $\mathbf{F}$, is derived from the incremental displacement field obtained by 2D digital image correlation. In the large scale framework implemented in the strain calculation code, the change in length and angle is represented by the right stretch tensor:

$$\mathbf{U} = \sqrt{\mathbf{F}^T \cdot \mathbf{F}} = \sqrt{\mathbf{U}^T \cdot \mathbf{R}^T \cdot \mathbf{R} \cdot \mathbf{U}} = \sqrt{\mathbf{U}^T \cdot \mathbf{U}} \tag{A.1}$$

where $\mathbf{R}$ is the antisymmetric part of $\mathbf{F}$, i.e. the rotation matrix, and "$\cdot$" denotes the inner product operator. This tensor is further decomposed into its isotropic and deviatoric multiplicative parts,

$$\mathbf{U} = \mathbf{U}_{iso} \cdot \mathbf{U}_{dev} \tag{A.2}$$

with

$$\mathbf{U}_{iso} = J^{1/2} \cdot \mathbf{I} \tag{A.3}$$

and

$$\mathbf{U}_{dev} = \frac{1}{J^{1/2}} \cdot \mathbf{U} \tag{A.4}$$

where J is the Jacobian, the determinant of $\mathbf{F}$, giving the change in volume between the initial and final configurations. Therefore, the two scalar quantities representing the volumetric and deviatoric deformations are respectively,

$$\epsilon_{vol} = J - 1 \tag{A.5}$$

and the Euclidean norm of deviatoric part of the stretch tensor,

$$\epsilon_{dev} = \|\mathbf{U}_{dev}\| \tag{A.6}$$

Appendix B. References

[1] A. Ord, I. Vardoulakis, R. Kajewski, Shear band formation in gosford sandstone, International Journal of Rock Mechanics and Mining Sciences & Geomechanics Abstracts 28 (1991) 397–409.

[2] L. Louis, T.-F. Wong, P. Baud, Imaging strain localization by X-ray radiography and digital image correlation: Deformation bands in Rothbach sandstone, Journal of Structural Geology 29 (2007) 129–140.

[3] P. Bésuelle, P. Baud, T.-F. Wong, Failure mode and spatial distribution of damage in Rothbach sandstone in the brittle-ductile transition, Pure and Applied Geophysics 160 (2003) 851–868.

[4] M. S. Paterson, T.-f. Wong, Experimental Rock Deformation-the Brittle Field, Springer Science & Business Media, 2005.

[5] T.-f. Wong, P. Baud, The brittle-ductile transition in porous rock: A review, Journal of Structural Geology 44 (2012) 25–53.

[6] M. Kwasniewski, X. Li, M. Takahashi, True Triaxial Testing of Rocks, volume 4, CRC Press, 2012.

[7] K. Mogi, Experimental Rock Mechanics, volume 3, CRC Press, 2006.

[8] M. Takahashi, H. Koide, Effect of the intermediate principal stress on strength and deformation behavior of sedimentary rocks at the depth shallower than 2000 m, in: Rock at Great Depth, International Society for Rock Mechanics, 1989.

[9] J. F. Labuz, F. Zeng, R. Makhnenko, Y. Li, Brittle failure of rock: A review and general linear criterion, Journal of Structural Geology 112 (2018) 7–28.

[10] B. Haimson, C. Chang, A new true triaxial cell for testing mechanical properties of rock, and its use to determine rock strength and deformability of Westerly granite, International Journal of Rock Mechanics and Mining Sciences 37 (2000) 285–296.

[11] B. C. Haimson, C. Chang, True triaxial strength of the KTB amphibolite under borehole wall conditions and its use to estimate the maximum horizontal in situ stress, Journal of Geophysical Research: Solid Earth 107 (2002).

[12] B. Haimson, J. W. Rudnicki, The effect of the intermediate principal stress on fault formation and fault angle in siltstone, Journal of Structural Geology 32 (2010) 1701–1711.

[13] M. Ingraham, K. Issen, D. Holcomb, Response of Castlegate sandstone to true triaxial states of stress, Journal of Geophysical Research: Solid Earth 118 (2013) 536–552.

[14] X. Ma, J. W. Rudnicki, B. C. Haimson, Failure characteristics of two porous sandstones subjected to true triaxial stresses: Applied through a novel loading path, Journal of Geophysical Research: Solid Earth 122 (2017) 2525–2540.

[15] P. Bésuelle, S. Hall, Characterization of the strain localization in a porous rock in plane strain condition using a new true-triaxial apparatus, in: Advances in Bifurcation and Degradation in Geomaterials, Springer, 2011, pp. 345–352.

[16] P. Bésuelle, P. Lanatà, A New True Triaxial Cell for Field Measurements on Rock Specimens and Its Use in the Characterization of Strain Localization on a Vosges Sandstone During a Plane Strain Compression Test, Geotechnical Testing Journal 39 (2016) 879–890.

[17] C. Couture, Mechanical Characterization of Porous Sandstones in True Triaxial Conditions: Diffuse and Localized Deformation, Effect of Anisotropy, Ph.D. thesis, Université Grenoble Alpes, Grenoble, France, 2020.

[18] P. Bésuelle, J. Desrues, S. Raynaud, Experimental characterisation of the localisation phenomenon inside a Vosges sandstone in a triaxial cell,

International Journal of Rock Mechanics and Mining Sciences 37 (2000) 1223–1237.

[19] J. F. Labuz, J. M. Bridell, Reducing Frictional Constraint in Compression Testing Through Lubrication, International Journal of Rock Mechanics and Mining Sciences 30 (1993) 451–455.

[20] R. P. Heilbronner, The autocorrelation function: an image processing tool for fabric analysis, Tectonophysics 212 (1992) 351–370.

[21] F. Hild, S. Roux, Digital image correlation: From displacement measurement to identification of elastic properties–a review, Strain 42 (2006) 69–80.

[22] M. Bornert, F. Brémand, P. Doumalin, J.-C. Dupré, M. Fazzini, M. Grédiac, F. Hild, S. Mistou, J. Molimard, J.-J. Orteu, L. Robert, Y. Surrel, P. Vacher, B. Wattrisse, Assessment of Digital Image Correlation Measurement Errors: Methodology and Results, Experimental Mechanics 49 (2009) 353–370.

[23] O. Stamati, E. Andò, E. Roubin, R. Cailletaud, M. Wiebicke, G. Pinzon, C. Couture, R. C. Hurley, R. Caulk, D. Caillerie, Spam: Software for Practical Analysis of Materials, Journal of Open Source Software 5 (2020) 2286.

[24] P. Bésuelle, Compacting and dilating shear bands in porous rock: Theoretical and experimental conditions, Journal of Geophysical Research 106 (2001) 13435–13442.

[25] A. Sornette, P. Davy, D. Sornette, Fault growth in brittle-ductile experiments and the mechanics of continental collisions, Journal of Geophysical Research: Solid Earth 98 (1993) 12111–12139.